Critical nucleus size for disease-related polyglutamine aggregation is repeat length dependent

Karunakar Kar[1,2], **Murali Jayaraman**[1,2], **Bankanidhi Sahoo**[1,2], **Ravindra Kodali**[1,2], and **Ronald Wetzel**[1,2]

[1]Structural Biology Department, University of Pittsburgh School of Medicine, Biomedical Sciences Tower 3, 3501 Fifth Avenue, Pittsburgh, PA 15260

[2]Pittsburgh Institute for Neurodegenerative Diseases, University of Pittsburgh School of Medicine, Biomedical Sciences Tower 3, 3501 Fifth Avenue, Pittsburgh, PA 15260

Abstract

Since polyglutamine (polyQ) aggregate formation has been implicated as playing an important role in expanded CAG repeat diseases, it is important to understand the biophysics underlying the initiation of aggregation. Previously we showed that relatively long polyQ peptides aggregate by nucleated growth polymerization and a monomeric critical nucleus. We show here that, over a short repeat length range from Q_{26} to Q_{23}, the size of the critical nucleus for aggregation increases from monomeric to dimeric to tetrameric. This variation in nucleus size suggests a common duplex anti-parallel β-sheet framework for the nucleus, and further supports the feasibility of an organized monomeric aggregation nucleus for longer polyQ repeat peptides. The data also suggest that a change in aggregation nucleus size may play a role in the pathogenicity of polyQ expansion in this series of familial neurodegenerative diseases.

Genetic expansion of a disease protein's polyglutamine (polyQ) sequence beyond repeat length thresholds in the 35–50 range is the defect underlying a series of expanded CAG repeat diseases including Huntington's disease 1. Amyloid-like neuronal polyQ aggregates are a pathological hallmark of these human neurodegenerative diseases 1,2, and polyQ aggregation rates exhibit a repeat length dependence in vitro 3,4 and in vivo 5. Understanding the physical basis of polyQ aggregation may therefore be a key requirement for understanding the molecular basis of disease. Deducing mechanisms by which amyloid growth is initiated, however, is technically challenging and is sometimes dependent on structural context. For example, we previously reported that simple polyQ sequences with pathological repeat lengths aggregate via a nucleated growth polymerization mechanism with a critical nucleus (n*) of one, without passing through any non-amyloid oligomeric intermediates 6,7. More recently, we found that the earlier reported 8,9 transient appearance

of oligomeric aggregates prior to amyloid formation in the aggregation of huntingtin (HTT) N-terminal fragments is due to the ability of the N-terminal 17 amino acid HTT^{NT} sequence to entirely alter the spontaneous aggregation mechanism [10]. Similar sequence context effects have been reported for several other polyQ proteins, both model sequences [11,12] and disease proteins [13,14], raising the issue of whether the physical behavior of simple polyQ peptides has any bearing on polyQ pathobiology.

In this paper we describe detailed aggregation kinetics studies of several polyQ-containing sequences that clarify this and other outstanding issues of polyQ biophysical behavior and its relation to disease. We show that the spontaneous aggregation of several disease-related, complex polyQ sequences, in analogy to simple polyQ peptides, is controlled by monomeric nucleus formation, suggesting that results from studies of polyQ model sequences are yielding data relevant to at least some polyQ pathology. We provide a detailed reanalysis of $K_2Q_{37}K_2$, and a detailed new analysis of $K_2Q_{23}K_2$, both of which confirm the absence of any detectable non-amyloid intermediates in their aggregation pathways. The $K_2Q_{37}K_2$ analysis establishes the robustness of the log-log slope value and confirms the previously reported [6] critical nucleus of one. In dramatic contrast, we find the critical nucleus for $K_2Q_{23}K_2$ to be four. Furthermore, by examining the intervening repeat length polyQs, we find a very sharp transition from $n^* = 4$ to $n^* = 1$ over the repeat length range Q_{23} to Q_{26}. The data validates the monomeric nucleation model for long polyQ sequences while suggesting a common folding motif for the critical nuclei for all polyQ peptides in the Q_{18} to Q_{47} repeat length range. The modest differences in nucleus size revealed in these studies project huge differences in the aggregation kinetics predicted for different repeat lengths at physiological concentrations.

Results

Flanking sequence effects on polyQ aggregation kinetics

Previously we showed that addition of a polyproline sequence to the C-terminal side of polyQ slows aggregation kinetics but does not change the nucleated growth / monomeric nucleus aggregation mechanism [15]. We also showed that placing the same polyproline sequence on the N-terminal side of polyQ changes neither aggregation rates nor mechanism [15]. In contrast, we found that the N-terminal 17 amino acids of the huntingtin protein (HTT^{NT}) situated directly adjacent to the polyQ sequence (Fig. 1a, top; Supplementary Fig. 1) dramatically alters the aggregation mechanism and increases the aggregation rate [10]. Hydrophobicity reducing mutations within HTT^{NT}, however, lead to partial to complete suppression of its rate-enhancing ability [10,16], suggesting that the rate-acceleration and mechanism-alteration by flanking sequences are far from universal, depending greatly on details of sequence.

To address whether polyQ flanking sequences from other expanded polyQ disease proteins might impart altered aggregation behavior onto polyQ sequences, we analyzed the impact of the N-terminus of the disease protein ataxin-7 (AT7) [1] on the aggregation of a Q_{30} sequence. This sequence exhibits interesting similarities and differences with the HTT^{NT} sequence of huntingtin, as brought out by an analysis (Methods) using the disorder predictor PONDR [17] (Fig. 1a). As in HTT, the polyQ sequence of AT7 lies near the N-terminus of the

protein and is followed by a short proline-rich sequence leading into a series of predicted ordered elements. As in HTT, the 29 amino acid N-terminal sequence of AT7 ("AT7^{NT}") leading into the polyQ sequence is predicted to have some tendency towards order (Fig. 1a). However, while the PONDR score of HTT^{NT} is well-below the 0.5 median normally associated with a tendency toward being structured 18, the PONDR score of AT7^{NT} falls above the 0.5 median, suggesting a negligible tendency toward order.

We obtained a peptide consisting of the AT7^{NT} sequence followed by a $Q_{30}K_2$ sequence. In contrast to the huge rate enhancement effect of HTT^{NT}, we found that, at comparable concentrations, AT7$^{NT}Q_{30}K_2$ aggregates somewhat slower than $K_2Q_{30}K_2$ (Fig. 1b). In addition, the aggregation kinetics of this peptide exhibited a concentration dependence (Fig. 1c) and linear time^2 plots (Fig. 1d) whose rates, as expected for nucleated growth polymerization reactions 19 increase with increasing starting monomer concentration (Fig. 1e). In fact, in good agreement with values obtained previously for simple polyQ peptides 6,7,15,20-22 and in contrast to values obtained for HTT^{NT}-containing polyQ sequences 10, the slope of the log-log plot of time^2 slopes vs. starting concentration (Fig. 1e) is 2.7, for an n* value of 0.7 (Table 1). DLS analysis showed no aggregate formation that was not detected by the sedimentation assay (Fig. 1f). Electron micrographs (Fig. 2) of the products of AT7$^{NT}Q_{30}K_2$ aggregation exhibit uniform, smooth-sided fibrils of $\sim$ 10 nm diameter and no discernable twist (Fig. 2a). Overall, the kinetic aggregation behavior of AT7$^{NT}Q_{30}K_2$ is more like that of simple polyQ peptides, and quite different from that of peptides containing the analogous HTT^{NT} sequence. While HTT N-terminal fragments aggregate via a two-step mechanism that includes non-nucleated, energetically downhill formation of non-amyloid oligomeric intermediates 10, the initial aggregation of AT7$^{NT}Q_{30}K_2$ is nucleated, with direct formation of amyloid aggregates, in analogy to the aggregation of simple polyQ peptides. These results are consistent with previous results 10,15 showing that not all polyQ disease protein flanking sequences alter polyQ aggregation mechanisms and kinetics.

Even for proteins like HTT that contain a flanking sequence that modifies mechanism, it is possible that proteolytic removal of all or part of the flanking sequence in the cell would generate a polyQ-containing fragment exhibiting the kinetic behavior of simple polyQ sequences. Isolated polyQ sequences are relatively resistant to proteolysis, even by the proteasome 23. In contrast, the HTT^{NT} sequence of HTT is sensitive to trypsin cleavage in monomeric HTT N-terminal fragments to generate a polyQ-containing fragment starting at Ser16 10 that may be biologically relevant (see Discussion). We obtained SFQ$_{37}P_{10}K_2$, the polyQ-containing product of trypsin cleavage of an HTT N-terminal peptide, and studied its aggregation properties. We found that, as expected, removal of the bulk of the HTT^{NT} sequence yields a peptide with aggregation kinetics that are greatly decreased compared with those for the peptide with intact HTT^{NT} (Fig. 3a). The time (Fig. 3b) and time^2 (Fig. 3c) plots for the aggregation of SFQ$_{37}P_{10}K_2$ exhibit a clear concentration dependence, as quantified by a log-log plot (Fig. 3d) giving a slope of 3.0, consistent with an n* of 1.0 (Table 1) and hence a monomeric nucleus. This slope of 3.0 is in stark contrast to analogous slopes for HTT N-terminal fragment peptides, which are in the range of one 10. EM images of the SFQ$_{37}P_{10}K_2$ aggregates (Fig. 2d) more resemble the products of simple polyQ aggregation ($K_2Q_{37}K_2$, Fig. 2b) than aggregated HTT N-terminal fragments (Fig. 2c). Collectively the data show that biologically feasible cleavage within the HTT^{NT} sequence

can produce a polyQ containing fragment whose aggregation properties more resemble those of simple polyQ sequences.

While flanking sequences have been described to play important modulating roles in the in vitro aggregation of some polyQ-containing proteins 10-14, details of the aggregation mechanisms of most polyQ disease proteins remain uncharacterized. PONDR analyses of these sequences shows that, in every case, the polyQ region of the sequence lies within extended segments that are predicted to be unstructured (Supplementary Figure 2). The unstructured nature of these flanking sequences suggests that (a) they may be more sensitive to proteolytic cleavage in the cell and (b) even if not cleaved they will be less likely, because of their low order propensity, to initiate an HTT^{NT}-like oligomerization mechanism.

Technical aspects of polyQ aggregation studies

To establish a benchmark for the studies on short polyQ peptides to be described later, we repeated a previous analysis of the peptide $K_2Q_{37}K_2$. This peptide was disaggregated using our normal protocol, and in addition the PBS solution of the peptide was filtered with a 20 nm membrane filter prior to incubation 24 (Methods). The peptide was incubated at 37 °C and aliquots removed and centrifuged, and the supernatant concentration measured by analytical HPLC to determine, by difference, the percent aggregation (Methods). For example, a 20 nm-filtered 25.5 ± 0.5 μM solution of $K_2Q_{37}K_2$, exhibiting no detectable DLS signal at t = 0, (Fig. 4a), was incubated. After 16 hrs, the solution continued to exhibit no detectable aggregates by DLS (Fig. 4a), and its concentration after 20 nm filtration was not appreciably changed (Supplementary Table 1). Detectable aggregation of this 25 μM solution was only observed, by the HPLC sedimentation assay, after 50 hrs (Fig. 4b). The aggregation kinetics data (Fig. 4b) yielded linear time^2 plots (Fig. 4c) and a linear log-log rate-concentration plot (Fig. 4d) giving a slope of 2.7 (Table 1) corresponding to n* = 0.7 (Table 1). These data were obtained using nine separate starting concentrations to yield a log-log plot with nine data points; the range of slopes obtained by calculating the slope from all possible 8-membered subsets of these data points is 2.52 – 2.85 (Table 1). The n* obtained is identical to the value of 0.7 obtained previously using only four starting concentrations of a monomer preparation that had not been subjected to the 20 nm filtration step 6.

Recently, Lee et al. conducted experiments with the peptide $K_2Q_{23}K_2$, which was disaggregated by a modification of our published protocol 25, stored frozen at high concentration in pH 3 water, then thawed, diluted, and incubated in PBS at 37 °C at 8–23 μM concentration. Monitoring the reactions by size exclusion chromatography, the authors reported a burst of monomer loss (interpreted as aggregation) equivalent to 30% of total incubated monomer within the first hour of incubation. The authors found that for a 23 μM solution these rapidly formed aggregates at two and six hrs had hydrodynamic radii of about 200 nm and masses of $47 – 126 \times 10^6$ Da, but exhibited no regular secondary structure (in particular, no β-sheet) 25. Since this report was not in agreement with our own findings on longer repeat lengths in the $K_2Q_NK_2$ series 6,7,20-22, we investigated the identical $K_2Q_{23}K_2$ sequence in our laboratory.

We disaggregated purified $K_2Q_{23}K_2$ by our standard protocol 26-28 and immediately incubated the resulting peptide at 52 μM in PBS at 37 °C, monitoring the reaction by the HPLC sedimentation assay. Surprisingly, after up to1400 hrs, no detectable aggregation occurred in this reaction (data not shown). Based on this result, we set up a repeat reaction at a significantly higher concentration of 215 μM, using peptide that, immediately before the initiation of incubation, had been subjected to our standard disaggregation procedure 28 and an additional 20 nm filtration (Methods). DLS analysis showed no detectable particles in this $K_2Q_{23}K_2$ solution, either at t = 0 or after 2 hrs incubation (Fig. 5a). The lack of appreciable formation of aggregates was confirmed by 20 nm membrane filtration, which showed that the concentration of filterable peptide after 2 hrs (214.4 ± 2.0 μM) was the same, within error, as the sample before incubation (214.9 ± 2.3 μM). Together these results indicate that aggregate formation after two hours incubation could not be detected by sedimentation assay, DLS or analytical membrane filtration, even though incubated at a starting concentration almost 10 times that previously reported to give 30% aggregation under similar conditions 25.

After the second membrane filtration of the two hours incubated sample, we incubated the 215 μM solution for an extended period at 37 °C and monitored aggregation by the HPLC sedimentation assay and by DLS. The results (Fig. 5b) show that the earliest detectable aggregate formation by sedimentation assay is at 20–24 hrs, at which times 1–3% of the monomer has been lost. In general agreement with this, the earliest DLS data rising reliably above buffer background is after 20 – 27 hrs incubation (Fig. 5b). At 27 hrs aggregation was at about 5% (Fig. 5b) and consisted of a broad distribution of particles with R_h values centered around 100 nm (Fig. 5c). At 52 hrs, about 42% of monomer has been converted into aggregate (sedimentation assay), and the intensity of the DLS autocorrelation function was high and did not reach baseline, which prevented deconvolution to obtain a size distribution (Fig. 5b). After 52 hrs, monomer continued to disappear from solution (Fig. 5b, gray bars), while the DLS signal became saturated, preventing the recording of data. The sensitivity of the DLS instrument was confirmed using IgM ($\sim 1 \times 10^6$ Da) as a standard. The IgM data (Fig. 5d) show that it takes a 16 μg/ml solution of IgM to achieve an equal amplitude to that observed when the 215 μM solution of $K_2Q_{23}K_2$ was 5% aggregated (i.e., approximately 32 μg/ml aggregates), consistent with the average aggregate at this time being roughly in the size range of IgM (1×10^6 Da).

The absence of non-amyloid aggregates during the lag time of aggregation was confirmed by EM analysis of the same reaction. No aggregates were observed at t = 0 (Fig. 2e). EM images taken at 24 hrs show only a very sparse distribution of aggregates (Fig. 2 f,g; see Fig. 2 legend), and these initially observed aggregates appear to be clusters of smaller versions of the later observed mature aggregates. In the following hours, aggregates remain sparsely distributed but become slightly longer (27 hrs, Fig. 2h), reaching a size range entirely consistent with the DLS result on the same sample (Fig. 5c). At later time points, where the sedimentation assay shows increased aggregation, EM grids are uniformly covered with longer fibrillar aggregates (Fig. 2 i-k). There is no apparent difference in morphology between aggregates of $K_2Q_{23}K_2$ (Fig. 2k) and $K_2Q_{37}K_2$ (Fig. 2b).

The sources of the discrepancies between these results for $K_2Q_{23}K_2$ and the previous report 25 are not clear. Possible factors include differences in the peptide sample, the disaggregation protocol, the handling of disaggregated peptides, and the aggregation buffer. It is clear, in any case, that in our hands aggregation of even very high concentrations of $K_2Q_{23}K_2$ is exceedingly slow and proceeds via amyloid-like structures. Not only was the aggregation much, much slower (even at much higher concentration), and of a different quality, than suggested by the results of Lee et al. 25, but aggregation was also much slower than expected based on our previous data for the slightly longer peptide $K_2Q_{28}K_2$ 6. This surprising result prompted us to take a closer examination of $K_2Q_{23}K_2$ aggregation kinetics.

Repeat length dependence of nucleus size

Working in the concentration range 103 – 227 μM, we carried out a concentration dependent aggregation kinetics analysis of $K_2Q_{23}K_2$. At 103 μM the peptide aggregates exceeding slowly for the first 120 hrs before beginning to aggregate rapidly (Fig. 6a, black squares). Consistent with a nucleated growth mechanism 29, aggregation of the same concentration of monomer is greatly enhanced in the presence of pre-formed seed (Fig 6a, blue, right pointing triangles). Also consistent with a nucleated growth mechanism 29, aggregation is reversible and exhibits a robust critical concentration of 3 μM (Fig. 6b). This is equivalent to a G_{elong} of − 7.8 kcal/mol, similar to the value of − 8.6 kcal/mol previously reported for Aβ(1–40) fibril formation 30. Consistent with nucleated growth polymerization, the initial phase of the aggregation kinetics exhibits a linear time^2 plot at each concentration tested 19 (Fig. 6c). When these time^2 rate slopes are plotted vs. starting concentration in a log-log plot (Fig. 6d), the results from the eight data points fit a straight line, as expected 6,19. However, in contrast with the slope values between 2.5 and 3 described above for $K_2Q_{37}K_2$ (Fig. 4d, Table 1) and found in every previous examination of simple polyQ sequences 6,7,15,20-22, the slope of this line is 5.9 (Table 1), corresponding to n* = 3.9.

Since the shortest simple polyQ peptide we have ever analyzed was a $K_2Q_{28}K_2$ peptide, which also exhibited an n* of about one 6, the value for the Q_{23} peptide indicated an abrupt change in n* over a relatively short repeat length range. To confirm this and to determine in detail how n* changes with respect to repeat length, we studied the intervening repeat lengths as well as a peptide with a repeat length well under Q_{23}. The detailed kinetics data for these studies are located in Supplementary Figure 3, while the log-log plots are shown in Figure 7 and the slope values and fitting parameters in Table 1.

Obtaining useful data for the peptide $K_2Q_{18}K_2$ required even higher concentrations (up to over 1 mM) than did the Q_{23} peptide (Supplementary Figure 3a). After analysis, n* for $K_2Q_{18}K_2$ was found to be also in the range of four (Fig. 7a; Table 1). We also examined the kinetics of peptides in the repeat length range Q_{24}–Q_{27} (Fig. 7; Supplementary Figure 3). We found that, as expected based on our prior examination of $K_2Q_{28}K_2$ 6, the $K_2Q_{27}K_2$ peptide exhibits a monomeric aggregation nucleus (Fig. 7b, Table 1). The Q_{26} peptide also has n* ∼ 1 (Fig. 7c, Table 1). In contrast, the Q_{25} peptide exhibits a slope of 4.0 (Fig. 7e) for n* = 2.0. The slope for the $K_2Q_{24}K_2$ peptide is 5.3, consistent with an n* of 3.3. The meaning of n* = 3.3 is not clear. The value may indicate a unique critical nucleus of three, or may be an intermediate value between n* = 2 and n* = 4 owing to both dimeric and

tetrameric nuclei being operational for this repeat length in this concentration range. Further analysis is required to better understand the nucleation mechanism for $K_2Q_{24}K_2$. Regardless of the interpretation of the Q_{24} data, it is clear there is a tight transition from a tetrameric critical nucleus, through a dimeric critical nucleus, to a monomeric critical nucleus as repeat length increases from Q_{23} to Q_{26} (Table 1). The aggregated products of each of these peptides are very similar by EM (Fig. 2k-p) and FTIR (Supplementary Figure 4).

Characteristics of the Q_{23} aggregation nucleus

To learn more about the $K_2Q_{23}K_2$ nucleated growth reaction, we evaluated the second order elongation rate constant and, from it, the nucleation equilibrium constant (Fig. 8). Thus, as previously described for other polyQ lengths [7,22,28], we conducted a seeded elongation reaction of $K_2Q_{23}K_2$ monomers containing a known weight concentration of previously prepared $K_2Q_{23}K_2$ fibrils to obtain a pseudo-first order rate constant for the elongation reaction (Fig. 8a). We determined the concentration of growing ends in the seed aggregate (Fig. 8b) [7,22,28] and used this value to calculate, from the pseudo-first order elongation (Fig. 8a) rate constant, a second order rate constant for elongation (k_+) of 1.24×10^4 $M^{-1}sec^{-1}$, which is almost identical to the previously reported value for a $K_2Q_{47}K$ peptide [7]. As previously discussed [7], such k_+ values fall well below the diffusion limit, possibly reflecting either the slow diffusion of the large reactants and/or the operation of a rate-limiting folding step (such as the "locking" phase of the dock-and-lock mechanism for fibril elongation [31] as part of the elongation cycle). Knowledge of k_+, along with the critical assumption that the elongation rate constant for fibrils is essentially the same as for nuclei, allowed us to calculate the nucleation equilibrium constant (K_{n*}) for $K_2Q_{23}K_2$ from the expression relating the y-intercept of the log-log plot (Fig. 6d) to the parameters k_+ and K_{n*}:

$$y-\text{intercept}=\log\left[\frac{1}{2}(k_+)^2 K_{n*}\right]$$

This analysis yields a value of K_{n*} for $K_2Q_{23}K_2$ of 7.6×10^{-2} l^3/mol^3. Using this value, we calculate that the concentration of tetrameric nucleus in pre-equilibrium with 100 μM monomer (a typical concentration in our aggregation experiments) is 7.6×10^{-18} M. Consistent with the slower nucleation of $K_2Q_{23}K_2$, this concentration is much lower than the steady state nucleus concentration of 2.6×10^{-13} M calculated for a 100 μM concentration of $K_2Q_{47}K_2$ from its previously determined K_{n*} [7]. Such values indicate the vanishingly small levels of the critical nucleus populated at any one time during nucleated growth, and thus illustrate the tremendous challenges in carrying out any type of structural or physical characterization of such kinetic nuclei [19].

Discussion

In the thermodynamic model for nucleated growth polymerization (Fig. 9), the nucleus is defined as the least stable species on the aggregation pathway [19,32]. Classically this critical nucleus (n*) is envisioned as a thermodynamically highly unfavorable multimer for which the subsequent docking of additional monomer units provides net stabilization (Fig. 9a). In precise analogy to the multimeric nucleus, the monomeric nucleus is also

thermodynamically unstable, representing a very small percentage of total monomer in solution. As with other nuclei in the formalism of the thermodynamic model, the overall efficiency of nucleation depends on both the steady-state concentration of the nucleus and the rate of its elongation [21]. In contrast with multimeric nuclei, however, the thermodynamic barrier to monomeric nucleus formation is solely dependent on conformational dynamics within the monomer ensemble [7]. We have envisioned this conformational change as an extremely unfavorable ordering, or folding, of polyQ into an elongation-competent structure that contains β-sheet elements in common with the final fibril structure (Fig. 9b) [7]. One prediction from this model is that, as repeat length gets shorter, a point might be reached where formation of such a metastable, ordered monomeric folding unit will be prohibitively unfavorable. We have been conducting studies to probe the robustness and range of the monomeric nucleation model [6,7,20-22].

There are nine different expanded polyQ repeat diseases, each with a different disease protein with different sequence elements flanking the polyQ tract [1]. In some cases, an adjacent element of structure dominates the initial stages of spontaneous aggregation in polyQ disease proteins [10,13,14]. However, the polyQ in most polyQ disease proteins is contained within a larger disordered segment (Fig. 1a, Supplementary Fig. 2) that may be susceptible to intracellular proteolysis, and/or may have no ability to independently aggregate. Thus, in contrast to the HTT [10] and AT3 [14] sequences, the AT7 N-terminal flanking sequence AT7^{NT} does not appear capable of triggering aggregation, or of appreciably altering the normal aggregation mechanism found for model polyQ peptides flanked by solubilizing Lys residues (Fig. 1). In fact, even the HTT^{NT} sequence does not entirely eliminate the previously described, normal polyQ aggregation mechanism. For example, we now know that the nucleation pathway previously described for simple polyQ sequences [6,7,15,20-22] contributes to overall aggregation of HTT^{NT} containing fragments (M. Jayaraman, A.K. Thakur, R. Mishra, R. Kodali and R. Wetzel, Ms. submitted) and may even be dominant if the HTT^{NT} sequence is bound to another protein [33] or is post-translationally modified [16]. Likewise, proteolytic cleavage at Lys15 within the HTT^{NT} sequence can take place in cells (A.L. Southwell, C.W. Bugg, L.S. Kaltenbach, D. Dunn, S.L. Butland, A. Weiss, P. Paganetti, D.C. Lo and P.H. Patterson, Ms. submitted), and full-length mutant HTT with 97Q carrying deletion of the HTT^{NT} domain has been found to still form aggregated mutant huntingtin in transgenic mouse brains (X. William Yang, David Geffen School of Medicine, UCLA, personal communication). We show here that the peptide produced when an HTT N-terminal fragment is cleaved at Lys15 aggregates according to the same nucleated growth polymerization mechanism, with $n^* = 1$, as previously found for similar repeat length versions of simple polyQ peptides (Fig. 3). Thus, further analysis of the nucleation mechanisms operative for simple polyQ peptides is not only relevant to fundamental characteristics of polymer assembly, but also to the biology of disease.

In our initial description of the classical nucleated growth polymerization behavior of simple polyQ sequences, we provided a body of data consistent with a simple, two-state transformation of monomeric coils to β-sheet rich amyloid-like aggregates, with no detectable alternatively structured intermediate aggregates, and with a surprising critical nucleus of one [6]. In the analyses described here, we build on this prior work but introduce

several modifications designed to provide additional confidence in the results. We introduced a 20 nm filtration step as an added measure to remove any pre-existing aggregates from starting monomer solutions, evaluated all kinetics time points in duplicate, and doubled the number of concentrations evaluated in the log-log plots. As described in Results, however, none of these changes made any appreciable difference in the previously obtained n* value for $K_2Q_{37}K_2$. By adding DLS measurements, time-dependent, semi-quantitative EM determinations, and an analytical 20 nm filtration analyses to test for the presence of even very small aggregates, we have not been able to observe the recently reported [25] formation of large amounts of large non-amyloid aggregates in the early stages of simple polyQ aggregation. Instead of the 30% monomer loss within two hours reported for 8–22 μM concentrations of $K_2Q_{23}K_2$ [25], we found < 1% loss of monomer for a 215 μM solution of the same peptide under the same conditions (Fig. 5, Supplementary Table 1).

The discovery that shorter polyQ peptides aggregate via the same general nucleated growth polymerization mechanism, but with larger critical nuclei, further supports our approach to data analysis [6,19] and the previously proposed monomeric nucleation pathway [6], and suggests that the latter is part of a continuum, linked by a common structural motif, that includes, for shorter polyQ lengths, higher order critical nuclei in the 2–4 range. Critical nuclei in this range have been reported previously for other amyloid formation reactions [34-37]. Recent studies of short polyQ peptides support a different aggregation mechanism mediated by formation of non-amyloid oligomers [38]. These peptides, however, are not only chemically different from those described here, but also were disaggregated and handled differently.

Being sparsely and transiently populated, it is essentially impossible – especially in a solution dominated by ground state molecules – to physically characterize the kinetic nucleus of a nucleated growth polymerization reaction [19]. Structural clues might be obtained by a number of means, however, such as molecular dynamics simulations [39,40], synthesis and testing of model peptides [41], or model building based on established structures of more stable intermediates or products. X-ray diffraction studies suggest that amyloid-like polyQ aggregates exist as slabs of β-sheets [42,43] with an anti-parallel chain arrangement [42]. Based on such structures, we hypothesize that the Q_{23} aggregation nucleus consists of four molecules of Q_{23}, each contributing one segment of extended chain, which are arranged as two stacked slabs, each slab consisting of two strands of anti-parallel sheet (Fig. 9d).

The identification of a multimeric nucleus for $K_2Q_{23}K_2$ aggregation has important implications for the structure of the monomeric nucleus for longer polyQs. One model for this structure is our previously described "folding" model [6,7] (Fig. 9b). However, since polyQ sequences exist in aqueous solution as compact coils [38,44] that appear to greatly resist expansion [45], the energetically unfavorable conformational change associated with nucleation might also be modeled as a rearrangement that transiently generates an isolated segment of solvated statistical coil (Fig. 9c). If this "statistical coil" model of the monomeric nucleus (Fig. 9c) were correct, however, we would expect that Q_{23} would also have an n* of 1, since solution structures with all or part of the chain in solvated, statistical coil seem likely to be more thermodynamically accessible to short polyQs than to longer polyQs [46].

Models such as that shown in Figure 9c are also inconsistent with other experimental data 22.

In contrast, a monomeric nucleus consisting of a highly organized, folded structure (Fig. 9b) is quite consistent with our model for the tetrameric nucleus for Q_{23} (Fig. 9d). Thus, the folded monomeric nucleus might structurally resemble the multimeric nucleus, except that all of the β-extended chain segments would now be derived from the same polypeptide sequence, through a series of turns and/or chain reversals (Fig. 9e). Consistent with this model, we previously reported that long, mutated polyQ peptides containing β-turn-favoring Pro-Gly pairs at regular intervals also aggregate via a monomeric nucleus, and that substitution with β-turn enhancing D-Pro-Gly pairs further accelerates aggregation 20. Furthermore, model building 47 and molecular dynamics simulations 48 suggest that structures like that shown in Figure 9e are feasible. Finally, it seems reasonable to conclude that the high degree of structural similarity in EMs (Fig. 2) and FTIR (Supplemental Fig. 4) between the Q_{23} and Q_{37} aggregates are ultimately derived from similarities in nucleus structure. A further extension of this logic suggests the structure shown in Figure 9f as a reasonable one for the dimeric critical nucleus implicated in the aggregation of $K_2Q_{25}K_2$ (Table 1).

Models of nucleus structure, however, are by definition speculative and can only be tested or refined, at best, indirectly. Nonetheless it is intriguing and possibly relevant that the nucleus sizes in these experiments tend to hover around low integer values (Table 1) and are largely consistent with reasonable structural models consistent with established principles of protein folding as well as data from structural and mutational analyses of polyQ aggregates. As critical nuclei, such structures, by definition, must be highly thermodynamically unfavorable 7 and therefore are not expected to represent the most highly populated conformation within the monomer ensemble in the kind of physical experiments described here. Such a low frequency of formation is consistent with the experimental 38,44,45 and computational 45,46 demonstration of the dominant presence of condensed, disordered forms within the monomer ensemble. Because of the rarity of the nucleus in this field of condensed states, it would appear that computer simulations that mirror polyQ solution behavior may be just as hard pressed as are solution measurements to identify, characterize and quantify the extremely rare kinetic nucleus. Perhaps the best one can hope to achieve is to survey and quantify the appearance of certain structural elements in MD simulations of polyQ peptide behavior 49, and to evaluate the energetics of hypothetical candidate nuclei 48.

It is important to stress that the model for the monomeric nucleus shown in Figure 9e is fundamentally different from reports of organized structures of polyQ proteins inferred from physical structural data and suggested to represent toxic, misfolded forms of polyQ 50. The calculated steady state concentration of the monomeric nucleus in a 1 nM concentration of $K_2Q_{47}K_2$ monomers is in the range of 10^{-18} M; the calculated concentration of the tetrameric nucleus in a 1 nM concentration of $K_2Q_{23}K_2$ is in the range of 10^{-37} M. It is not feasible that these critical nuclei at such low concentrations might be directly toxic to cells. If aggregation critical nucleus structures are, in fact, associated with any disease-related toxicity, the effects must indirect, bestowed by virtue of their abilities to stimulate and mediate the rapid growth of toxic polyQ aggregates.

In fact, the rather small differences in nucleus size described here have enormous consequences for projected aggregation kinetics. Extrapolation of our data (obtained through experiments in the μM range) into the nM range of concentrations that are more likely to obtain in cells suggests a potentially huge difference in nucleation rates between Q_{23} and Q_{37} sequences due to the difference in their concentration dependence (Fig. 8c). A simulation (Fig. 8d) using parameters derived from the nucleation kinetics analysis underscores the power of this apparently modest slope difference, indicating that, while in vitro incubation at 1 nM would be expected to yield Q_{37} aggregation in 10–100 years, Q_{23} aggregation is expected to begin taking place only after 10–100 billion years! These extrapolations are shown only to illustrate the potential power of nucleus size to control aggregation propensity. The assumption of linearity over large concentration differences that underlie the extrapolations may well not be justified; it is possible that at some low polyQ concentration a nucleus of different size and associated kinetics might become more favored.

The complexity of aggregation nucleation revealed here introduces fascinating new issues for polyQ aggregation nucleated growth, including how repeat length effects on aggregation relate to repeat length effects on disease risk. Although the results reveal an extremely tight transition in the relationship between repeat length and nucleus size that is reminiscent of sharp transitions in curves of disease risk and repeat length 1, the repeat length threshold for nucleus size change revealed by our studies is 24–25, while thresholds for disease risk tend to be in the 35–45 range (note, however, the single exception of the disease spinocerebellar ataxia 6, for which the repeat length threshold is between 18 and 21 Q) 1. Is there a molecular basis for the difference between these analogously sharp, but non-overlapping, thresholds? The data presented here provide new hope for improved understanding of the connections between the repeat length dependence of disease risk and the repeat length dependence of polyQ physical properties, with implications for the prospects for discovering disease mechanisms and therapeutics.

Methods

Handling of peptides

Crude synthetic peptides were obtained from the Keck Biotechnology Resource Laboratory of Yale University (http://keck.med.yale.edu/), purified to homogeneous repeat lengths by reverse phase chromatography, and the structures and purities confirmed by LC-MS on an Agilent mass spectrometer. Lyophilized pure peptides were disaggregated as described 28 using a 16 hrs incubation in a 1:1 mixture of trifluoroacetic acid (TFA, Pierce) and hexafluoroisopropanol (HFIP, Acros Organics), followed by evaporation of solvent under nitrogen, exposure to vacuum, dissolving in pH 3 TFA-H_2O, and high speed centrifugation. The top 80% of the supernatant was removed and its concentration determined by HPLC 28. Such stock solutions were always prepared fresh, rather than stored frozen, since storage of polyglutamine peptides in frozen aqueous solution can lead to substantial aggregation due to freeze concentration effects 28,51. Final solutions for aggregation studies at each peptide concentration were prepared by adding 1/9 volume of a 10× PBS buffer concentrate,

followed by mixing. Most starting peptide solutions were also filtered through a 20 nm filter unit (Anotop 10, Whatman).

Sedimentation assay

Time points were analyzed in duplicate by removing aliquots and centrifuging at $20,800 \times g$ for 45 mins, then carefully sampling the supernatant and injecting into the analytical HPLC 28. The peak area corresponding to the peptide was integrated and the number of μg peptide read off a standard curve 28. All aggregation kinetics data shown in this paper were conducted in 0.05% (w/v) sodium azide in PBS at 37 °C and were monitored by the sedimentation assay.

Preparing and quantifying seed aggregates

Seed aggregates for $K_2Q_{23}K_2$ were prepared and quantified as previously described 28. After the $K_2Q_{23}K_2$ aggregation had gone nearly to completion, aggregates were collected and washed by centrifugation ($20,800 \times g$), then resuspended in PBS. An aliquot of the suspension was dissolved in 100% formic acid and injected into HPLC, with the integrated peak converted to μg $K_2Q_{23}K_2$ using a standard curve. From this measurement the weight concentration of the seed suspension was calculated. Growing end titrations of seeds using biotinyl-$K_2Q_{29}K_2$ were conducted as described 7,28.

Determination of the C_r and the reversibility of aggregate formation

A forward aggregation reaction of $K_2Q_{23}K_2$ was monitored by the sedimentation assay until the % monomer exhibited no further change. Meanwhile, a late time point aliquot of an aggregation reaction was diluted into PBS such that the total $K_2Q_{23}K_2$ concentration was well above the approximate C_r while the remaining monomer concentration was well below the approximate C_r. This was incubated at 37 °C and the amount of monomer in the supernatant periodically determined, using the sedimentation assay, until the % monomer value stabilized. For details, see 28,30.

Nucleation kinetics analysis and simulated aggregation curves

Aggregation kinetics data were treated as described previously 6,28, using the equation = $\frac{1}{2}(k_+^2)(K_{n*}) c^{(n*+2)}t^2$, in which is the molar concentration of monomers that has been converted to aggregates at time t, and k_+ is the second order elongation rate constant for nucleus elongation and aggregate elongation (which are assumed to be identical), c is the molar concentration of monomers at the start of the reaction, $n*$ is the critical nucleus (the number of monomers that associate together to form the nucleus), and K_{n*} is the nucleation equilibrium constant. The slope of the log-log plot (Figure 2B) = $n* + 2$. The y intercept of the plot = $\log [\frac{1}{2}(k_+^2)(K_{n*})]$. Using the equation and these values it is also possible to calculate simulated aggregation curves for experimentally inaccessible concentrations. The use of the y intercept and second order elongation rate constant to calculate K_{n*} is described in the text and in previous publications 7,28.

Electron microscopy

An aliquot of 5 μl from the ongoing aggregation reaction mixture at different time points was placed on freshly glow-discharged carbon coated 400 mesh size copper grids, adsorbed for 2 min, and the grid washed with a drop of deionized water, before staining the sample with freshly filtered 5μl of 1% (w/v) uranyl acetate for 2 sec. The excess of sample, washes and stains was gently blotted off with filter paper. Grids were imaged in the Structural Biology Department's EM facility on a Tecnai T12 microscope (FEI) operating at 120 kV and 30,000 × magnification and equipped with an UltraScan 1000 CCD camera (Gatan) with post-column magnification of 1.4 ×.

FTIR

Fourier transform infrared spectroscopy of final aggregates was carried out on an MB3000 series spectrophotometer (ABB) with PROTA software (BioTools, Inc.). Peptide aggregates were collected by centrifugation at $20,800 \times g$ and the pellet was washed three times with PBS. Spectra were recorded at 4 cm^{-1} resolution (400 scans at room temperature) and corrected for the residual buffer absorption by subtracting the buffer-alone spectrum interactively until a flat baseline was obtained in the $1,700$–$1,800$ cm^{-1} region. Second-derivative spectra for the Amide I region were calculated using PROTA software.

Dynamic light scattering

DLS measurements were performed at 37 °C using DynaPro plate reader (Wyatt Technology Corp.) equipped with a temperature controller. An aliquot of ~75μl was directly transferred from the ongoing reaction mixture at different time points to a fresh well of a 384 micro plate to record the scattering data. Dynamics V6 software (Wyatt Technology Corp.) was used to process the data and to analyze the autocorrelation functions to obtain the hydrodynamic radii (R_h).

Order analysis

Sequence-based predictions of protein order were calculated using the VX-LT (copyright©1999 by the WSU Research Foundation, all rights reserved) version of PONDR (PONDR® is copyright©2004 by Molecular Kinetics, all rights reserved).

Data analysis

Where error bars are shown, results are s.d. from analyses in duplicate. For simplicity error bars are not added to the monomer concentration data in the $time^2$ plots but are only shown in the time plots. For all the reaction profiles, data sets were fit in Origin 7.5 software (OriginLab Corporation). The time plots were fit to B-spline curves. The $time^2$ plots and log-log plots were fit by linear regression. Growth site measurements data shown in Figure 8b were fit to sigmoidal.

Supplementary Material

Refer to Web version on PubMed Central for supplementary material.

Acknowledgments

References

1. Bates, GP.; Benn, C. The polyglutamine diseases. In: Bates, GP.; Harper, PS.; Jones, L., editors. Huntington's Disease. Oxford University Press; Oxford, U.K.: 2002. p. 429-472.

2. Ross CA, Poirier MA. Opinion: What is the role of protein aggregation in neurodegeneration? Nat Rev Mol Cell Biol. 2005; 6:891–8. [PubMed: 16167052]

3. Scherzinger E, et al. Huntingtin-encoded polyglutamine expansions form amyloid-like protein aggregates in vitro and in vivo. Cell. 1997; 90:549–58. [PubMed: 9267034]

4. Chen S, Berthelier V, Yang W, Wetzel R. Polyglutamine aggregation behavior *in vitro* supports a recruitment mechanism of cytotoxicity. J Mol Biol. 2001; 311:173–182. [PubMed: 11469866]

5. Davies SW, et al. Formation of neuronal intranuclear inclusions underlies the neurological dysfunction in mice transgenic for the HD mutation. Cell. 1997; 90:537–48. [PubMed: 9267033]

6. Chen S, Ferrone F, Wetzel R. Huntington's Disease age-of-onset linked to polyglutamine aggregation nucleation. Proc Natl Acad Sci USA. 2002; 99:11884–11889. [PubMed: 12186976]

7. Bhattacharyya AM, Thakur AK, Wetzel R. polyglutamine aggregation nucleation: thermodynamics of a highly unfavorable protein folding reaction. Proc Natl Acad Sci U S A. 2005; 102:15400–5. [PubMed: 16230628]

8. Poirier MA, et al. Huntingtin spheroids and protofibrils as precursors in polyglutamine fibrilization. J Biol Chem. 2002; 277:41032–7. [PubMed: 12171927]

9. Wacker JL, Zareie MH, Fong H, Sarikaya M, Muchowski PJ. Hsp70 and Hsp40 attenuate formation of spherical and annular polyglutamine oligomers by partitioning monomer. Nat Struct Mol Biol. 2004; 11:1215–22. [PubMed: 15543156]

10. Thakur AK, et al. Polyglutamine disruption of the huntingtin exon 1 N terminus triggers a complex aggregation mechanism. Nat Struct Mol Biol. 2009; 16:380–9. [PubMed: 19270701]

11. Bulone D, Masino L, Thomas DJ, San Biagio PL, Pastore A. The Interplay between PolyQ and Protein Context Delays Aggregation by Forming a Reservoir of Protofibrils. PLoS ONE. 2006; 1:e111. [PubMed: 17205115]

12. Ignatova Z, Thakur AK, Wetzel R, Gierasch LM. In-cell aggregation of a polyglutamine-containing chimera is a multistep process initiated by the flanking sequence. J Biol Chem. 2007; 282:36736–43. [PubMed: 17942400]

13. de Chiara C, Menon RP, Dal Piaz F, Calder L, Pastore A. Polyglutamine is not all: the functional role of the AXH domain in the ataxin-1 protein. J Mol Biol. 2005; 354:883–93. [PubMed: 16277991]

14. Ellisdon AM, Thomas B, Bottomley SP. The two-stage pathway of ataxin-3 fibrillogenesis involves a polyglutamine-independent step. J Biol Chem. 2006; 281:16888–96. [PubMed: 16624810]

15. Bhattacharyya A, et al. Oligoproline effects on polyglutamine conformation and aggregation. J Mol Biol. 2006; 355:524–35. [PubMed: 16321399]

16. Gu X, et al. Serines 13 and 16 are critical determinants of full-length human mutant huntingtin induced disease pathogenesis in HD mice. Neuron. 2009; 64:828–40. [PubMed: 20064390]

17. Romero P, Obradovic Z, Dunker AK. Natively disordered proteins: functions and predictions. Appl Bioinformatics. 2004; 3:105–13. [PubMed: 15693736]

18. Mohan A, et al. Analysis of molecular recognition features (MoRFs). J Mol Biol. 2006; 362:1043–59. [PubMed: 16935303]

19. Ferrone F. Analysis of protein aggregation kinetics. Meths Enzymol. 1999; 309:256–274.

20. Thakur A, Wetzel R. Mutational analysis of the structural organization of polyglutamine aggregates. Proc Natl Acad Sci U S A. 2002; 99:17014–17019. [PubMed: 12444250]

21. Slepko N, et al. Normal-repeat-length polyglutamine peptides accelerate aggregation nucleation and cytotoxicity of expanded polyglutamine proteins. Proc Natl Acad Sci U S A. 2006; 103:14367–72. [PubMed: 16980414]

22. Jayaraman M, Kodali R, Wetzel R. The impact of ataxin-1-like histidine insertions on polyglutamine aggregation. Protein Eng Des Sel. 2009; 22:469–78. [PubMed: 19541676]

23. Venkatraman P, Wetzel R, Tanaka M, Nukina N, Goldberg AL. Eukaryotic proteasomes cannot digest polyglutamine sequences and release them intact during degradation of polyglutamine-containing proteins. Mol Cell. 2004; 14:95–104. [PubMed: 15068806]

24. Kirkitadze MD, Condron MM, Teplow DB. Identification and characterization of key kinetic intermediates in amyloid beta-protein fibrillogenesis. J Mol Biol. 2001; 312:1103–19. [PubMed: 11580253]

25. Lee CC, Walters RH, Murphy RM. Reconsidering the mechanism of polyglutamine Peptide aggregation. Biochemistry. 2007; 46:12810–20. [PubMed: 17929830]

26. Chen S, Wetzel R. Solubilization and disaggregation of polyglutamine peptides. Protein Science. 2001; 10:887–891. [PubMed: 11274480]

27. Wetzel, R. Protein folding and aggregation in the expanded polyglutamine repeat diseases. In: Buchner, J.; Kiefhaber, T., editors. The Protein Folding Handbook. Part II. Wiley-VCH; Weinheim: 2005. p. 1170-1214.

28. O'Nuallain B, et al. Kinetics and thermodynamics of amyloid assembly using a high-performance liquid chromatography-based sedimentation assay. Methods Enzymol. 2006; 413:34–74. [PubMed: 17046390]

29. Frieden C. Protein aggregation processes: In search of the mechanism. Protein Sci. 2007; 16:2334–44. [PubMed: 17962399]

30. O'Nuallain B, Shivaprasad S, Kheterpal I, Wetzel R. Thermodynamics of abeta(1-40) amyloid fibril elongation. Biochemistry. 2005; 44:12709–18. [PubMed: 16171385]

31. Cannon MJ, Williams AD, Wetzel R, Myszka DG. Kinetic analysis of beta-amyloid fibril elongation. Anal Biochem. 2004; 328:67–75. [PubMed: 15081909]

32. Ferrone FA. Nucleation: the connections between equilibrium and kinetic behavior. Methods Enzymol. 2006; 412:285–99. [PubMed: 17046664]

33. Tam S, et al. The chaperonin TRiC blocks a huntingtin sequence element that promotes the conformational switch to aggregation. Nat Struct Mol Biol. 2009; 16:1279–85. [PubMed: 19915590]

34. Arvinte, T. Human calcitonin fibrillogenesis. In: Bock, GR., editor. The Nature and Origin of Amyloid Fibrils; Ciba Foundation Symposium 199. Wiley; New York: 1996. p. 90-97.

35. Collins SR, Douglass A, Vale RD, Weissman JS. Mechanism of prion propagation: amyloid growth occurs by monomer addition. PLoS Biol. 2004; 2:e321. [PubMed: 15383837]

36. Frankenfield KN, Powers ET, Kelly JW. Influence of the N-terminal domain on the aggregation properties of the prion protein. Protein Sci. 2005; 14:2154–66. [PubMed: 16046631]

37. Xue WF, Homans SW, Radford SE. Systematic analysis of nucleation-dependent polymerization reveals new insights into the mechanism of amyloid self-assembly. Proc Natl Acad Sci U S A. 2008; 105:8926–31. [PubMed: 18579777]

38. Walters RH, Murphy RM. Examining polyglutamine peptide length: a connection between collapsed conformations and increased aggregation. J Mol Biol. 2009; 393:978–92. [PubMed: 19699209]

39. Khare SD, Ding F, Gwanmesia KN, Dokholyan NV. Molecular origin of polyglutamine aggregation in neurodegenerative diseases. PLoS Comput Biol. 2005; 1:230–5. [PubMed: 16158094]

40. Marchut AJ, Hall CK. Effects of chain length on the aggregation of model polyglutamine peptides: molecular dynamics simulations. Proteins. 2007; 66:96–109. [PubMed: 17068817]

41. Smith MH, et al. Polyglutamine fibrils are formed using a simple designed beta-hairpin model. Proteins. 2010; 78:1971–9. [PubMed: 20408173]

42. Sharma D, Shinchuk LM, Inouye H, Wetzel R, Kirschner DA. Polyglutamine homopolymers having 8-45 residues form slablike beta-crystallite assemblies. Proteins. 2005; 61:398–411. [PubMed: 16114051]

43. Sikorski P, Atkins E. New model for crystalline polyglutamine assemblies and their connection with amyloid fibrils. Biomacromolecules. 2005; 6:425–32. [PubMed: 15638548]

44. Crick SL, Jayaraman M, Frieden C, Wetzel R, Pappu RV. Fluorescence correlation spectroscopy shows that monomeric polyglutamine molecules form collapsed structures in aqueous solutions. Proc Natl Acad Sci U S A. 2006; 103:16764–9. [PubMed: 17075061]

45. Dougan L, Li JY, Badilla CL, Berne BJ, Fernandez JM. Single homopolypeptide chains collapse into mechanically rigid conformations. Proc Natl Acad Sci U S A. 2009; 106:12605–12610. [PubMed: 19549822]

46. Wang X, Vitalis A, Wyczalkowski MA, Pappu RV. Characterizing the conformational ensemble of monomeric polyglutamine. Proteins. 2006; 63:297–311. [PubMed: 16299774]

47. Starikov EB, Lehrach H, Wanker EE. Folding of oligoglutamines: a theoretical approach based upon thermodynamics and molecular mechanics. J Biomol Struct Dyn. 1999; 17:409–27. [PubMed: 10636078]

48. Esposito L, Paladino A, Pedone C, Vitagliano L. Insights into structure, stability, and toxicity of monomeric and aggregated polyglutamine models from molecular dynamics simulations. Biophys J. 2008; 94:4031–40. [PubMed: 18234827]

49. Lakhani VV, Ding F, Dokholyan NV. Polyglutamine induced misfolding of huntingtin exon1 is modulated by the flanking sequences. PLoS Comput Biol. 2010; 6:e1000772. [PubMed: 20442863]

50. Nagai Y, et al. A toxic monomeric conformer of the polyglutamine protein. Nat Struct Mol Biol. 2007; 14:332–40. [PubMed: 17369839]

51. Chen S, Berthelier V, Hamilton JB, O'Nuallain B, Wetzel R. Amyloid-like features of polyglutamine aggregates and their assembly kinetics. Biochemistry. 2002; 41:7391–9. [PubMed: 12044172]
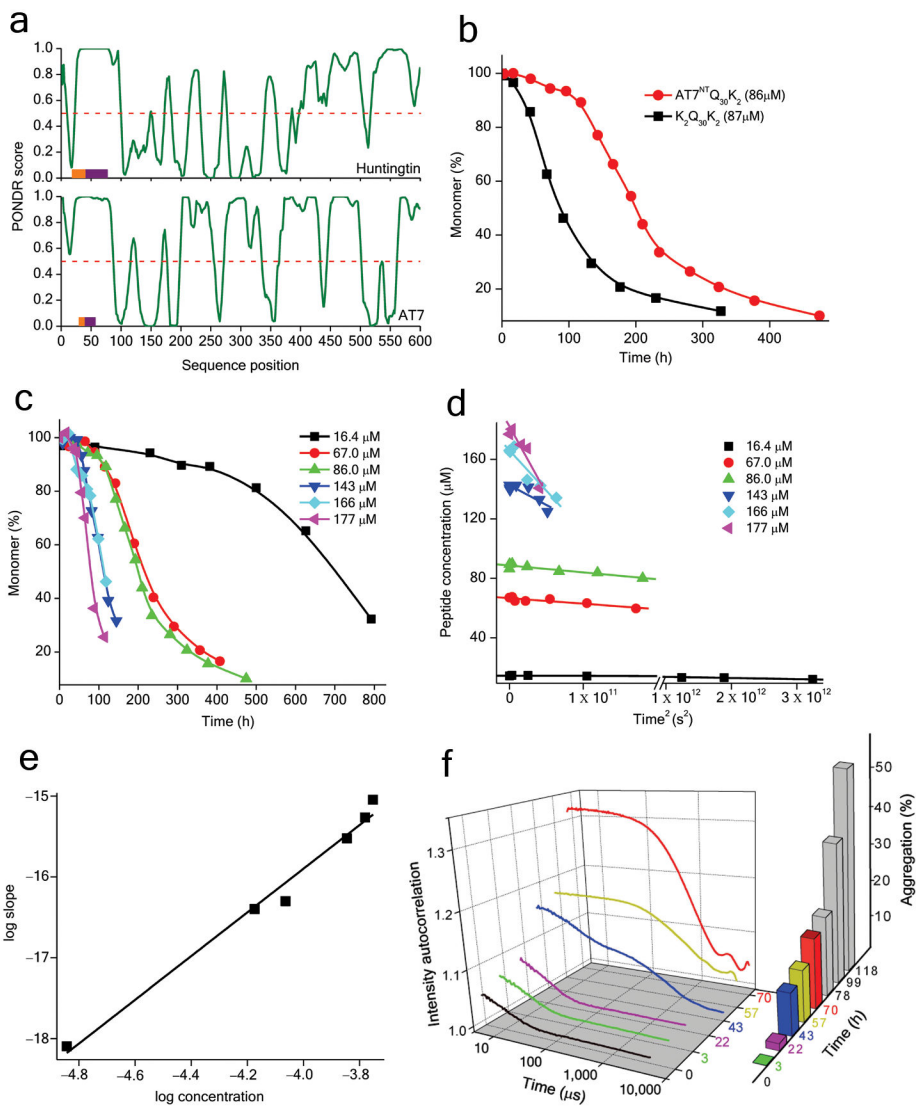
Figure 1.
Effect of AT7[NT] on polyQ aggregation kinetics. a. PONDR analysis of first 600 amino acids of the human HTT and AT7 sequences. Scores between 0.5 and 1 are associated with disorder; scores between 0 and 0.5 with order. The orange bars represent the polyQ sequence; the purple bars the Pro-rich sequence. b. Comparison of aggregation kinetics of peptide AT7[NT]$Q_{30}K_2$ and $K_2Q_{30}K_2$. c. Aggregation kinetics of different concentrations of AT7[NT]$Q_{30}K_2$. d. Initial aggregation kinetics data of AT7[NT]$Q_{30}K_2$ from part c plotted against time^2. e. Log-log plots of initial reaction rates (from part d) versus initial concentration for AT7[NT]$Q_{30}K_2$. f. Autocorrelation functions obtained from DLS measurements at different incubation times of the aggregation reaction of AT7[NT]$Q_{30}K_2$ at 166 μM, along with a histogram of the percent aggregation at the same time points derived from HPLC/sedimentation analysis.
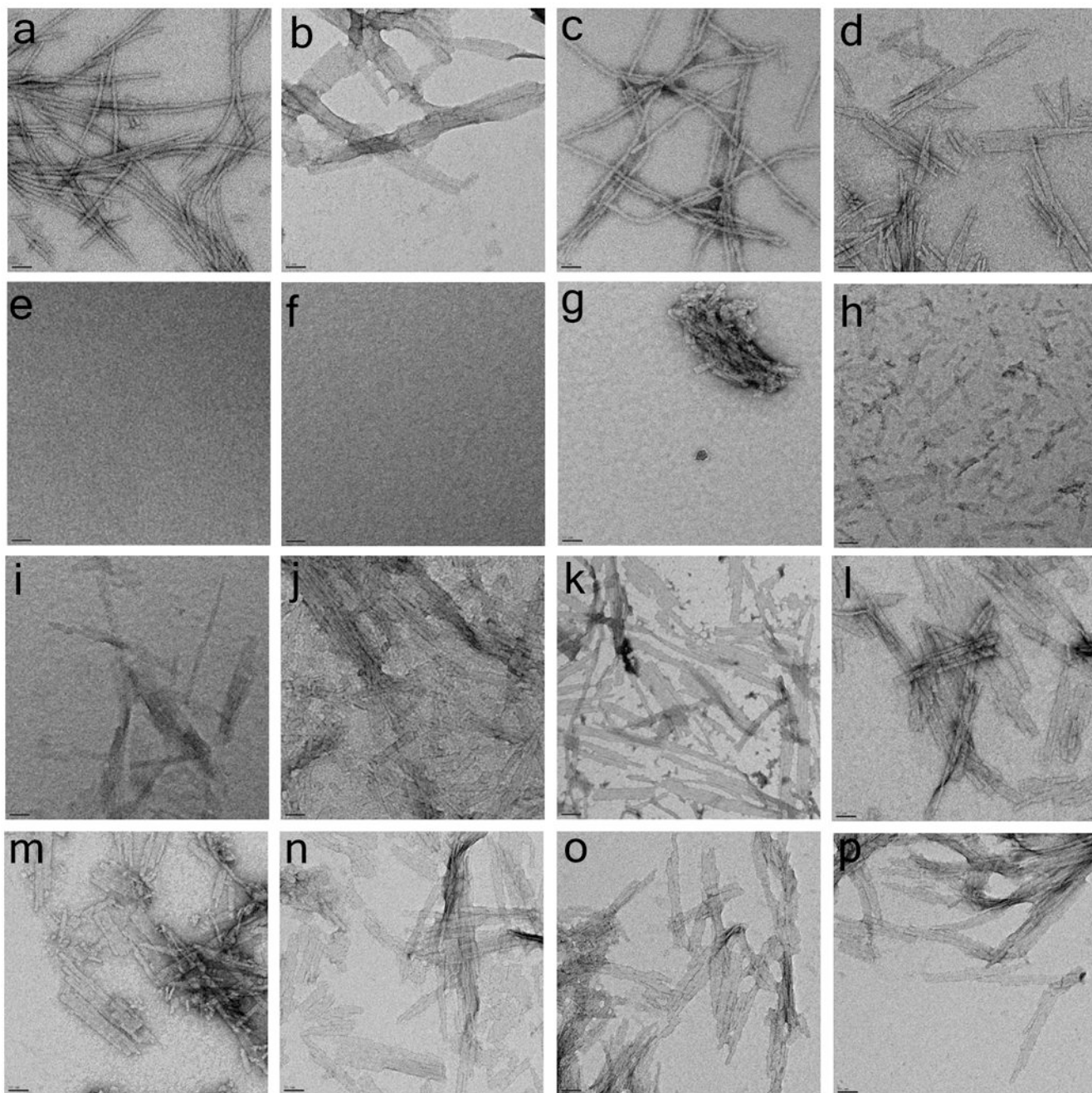
Figure 2.
Transmission electron micrograph images obtained for different peptides incubated in PBS at 37°C. Shown are the end-stage aggregates of $AT7^{NT}Q_{30}K_2$ (a), $K_2Q_{37}K_2$ (b), $HTT^{NT}Q_{37}P_{10}K_2$ (c), $SFQ_{37}P_{10}K_2$ (d), $K_2Q_{18}K_2$ (l), $K_2Q_{24}K_2$ (m), $K_2Q_{25}K_2$ (n), $K_2Q_{26}K_2$ (o), and $K_2Q_{27}K_2$ (p). Also shown are representative images from different incubation times of a 215 μM reaction of $K_2Q_{23}K_2$ observed at 0 hrs (e), 24 hrs (f, g), 27 hrs (h), 36 hrs (i), 52 hrs (j), and 200 hrs (k). The vast proportion of the EM grid examined for the 24 hrs time point for $K_2Q_{23}K_2$ aggregation resembled part f (no visible aggregate). Scale bar = 50 nm.
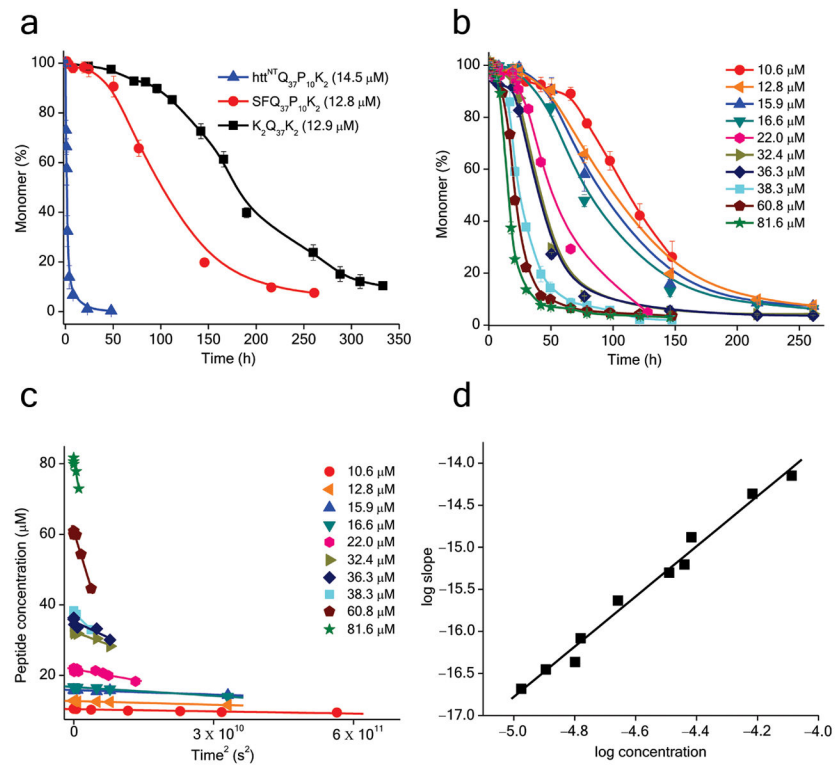
Figure 3.
Aggregation kinetics analysis of the peptide $SFQ_{37}P_{10}K_2$. a. Comparison of aggregation kinetics of $HTT^{NT}Q_{37}P_{10}K_2$, $SFQ_{37}P_{10}K_2$ and $K_2Q_{37}K_2$. b. Aggregation kinetics for $SFQ_{37}P_{10}K_2$ at different concentrations. c. Initial aggregation kinetics data of $SFQ_{37}P_{10}K_2$ from part b plotted against $time^2$. d. Log-log plot of initial reaction rates (slopes from part c) versus initial concentration for $SFQ_{37}P_{10}K_2$.
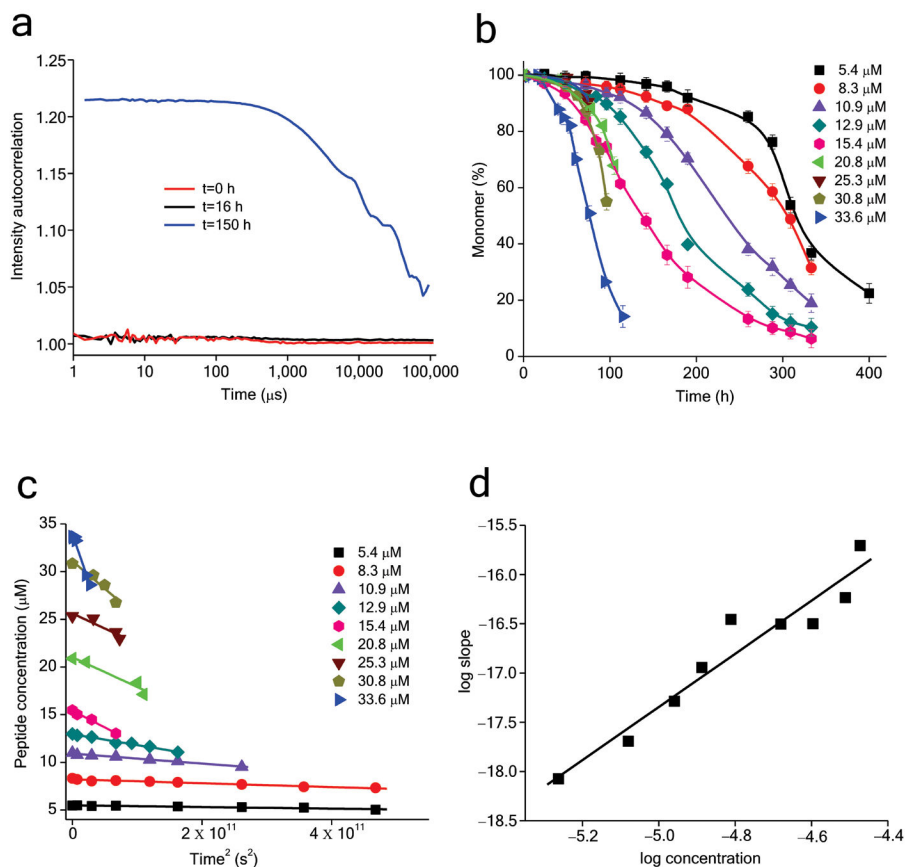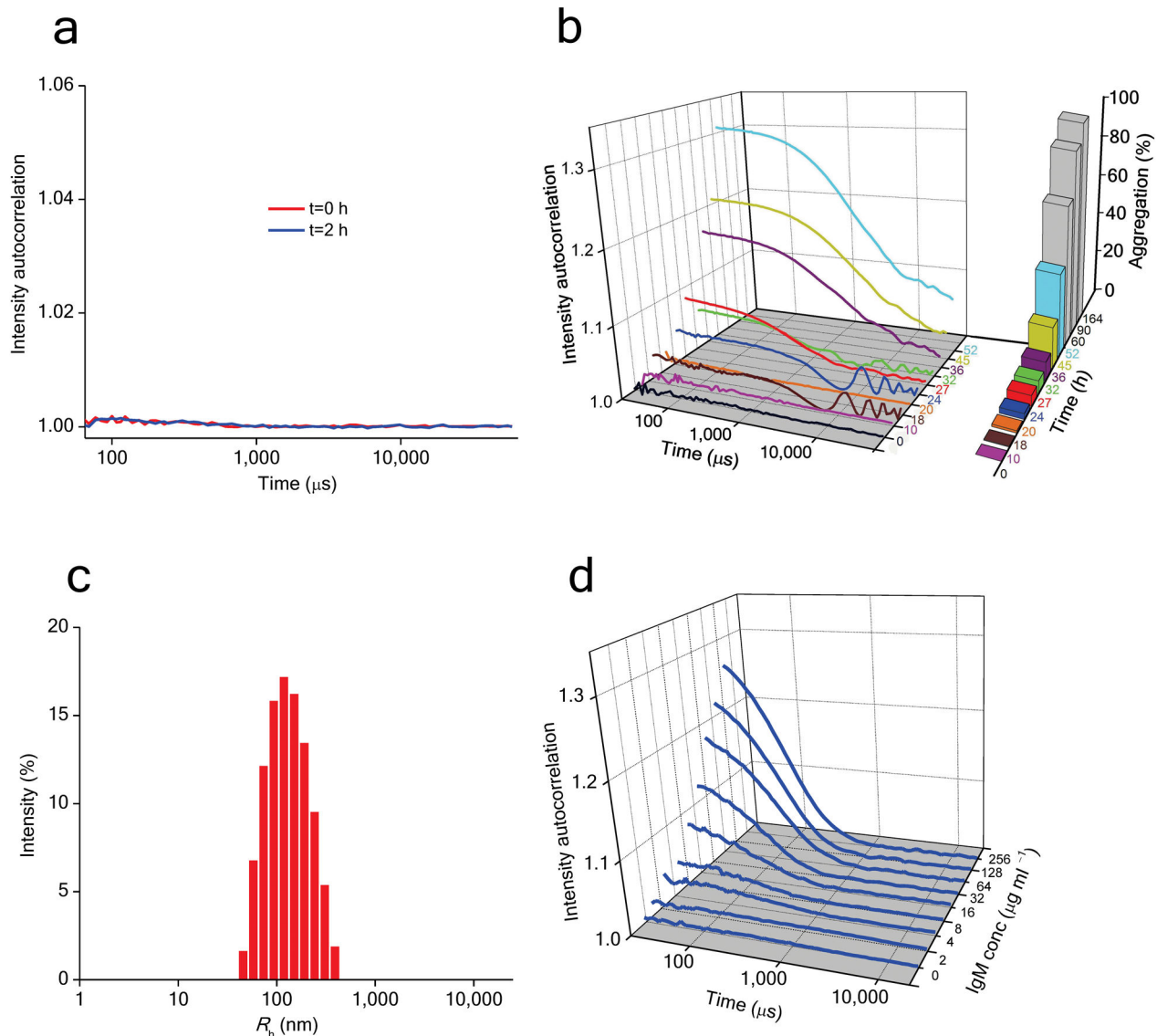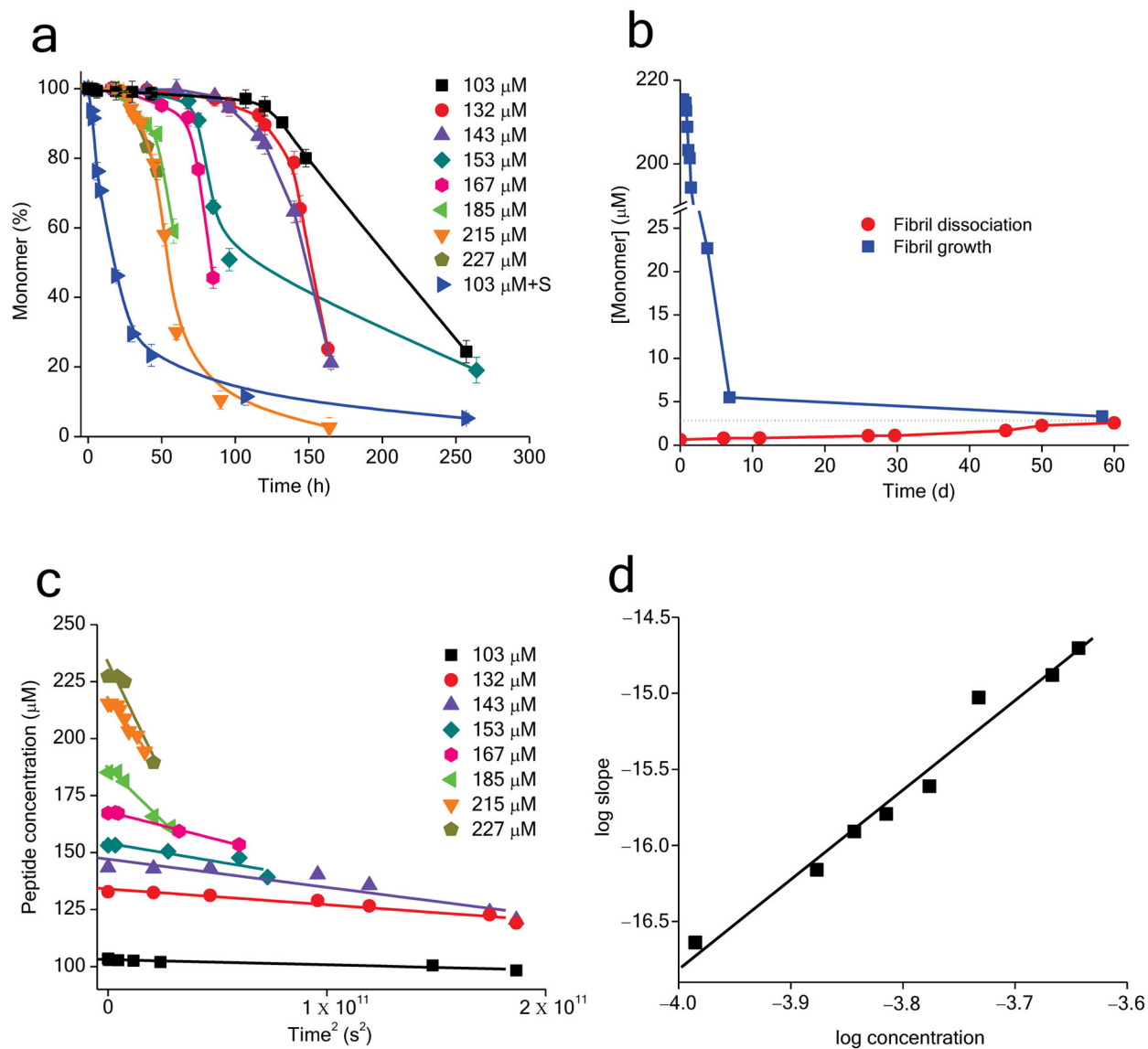
Figure 4.
Aggregation kinetics of peptide $K_2Q_{37}K_2$ in PBS at 37°C. a. DLS measurements of the aggregation reaction mixture of $K_2Q_{37}K_2$ at 25.5 μM starting concentration at the times indicated. b. Aggregation kinetics for $K_2Q_{37}K_2$ at different concentrations. c. Initial aggregation kinetics data of $K_2Q_{37}K_2$ from part b plotted against time^2. d. Log-log plots of initial reaction rates (slopes from part c) versus initial concentration for $K_2Q_{37}K_2$.

Figure 5.
DLS analysis of the aggregation reaction of $K_2Q_{23}K_2$ at 215 μM. a. Autocorrelation functions obtained on freshly disaggregated and filtered 215 μM solution of $K_2Q_{23}K_2$ (0 h) and after 2 hours incubation at 37 °C in PBS. b. Autocorrelation functions on the aggregation reaction of the 2 hours reaction from part a, after first being subjected to a second 20 nm filtration (even though there is no indication of aggregate formation by DLS or by material loss on filtration; see Results). Also shown for this 215 μM reaction is a histogram of the percent aggregation at the same time points derived from HPLC/sedimentation analysis. c. Hydrodynamic radius (R_h) derived from the DLS data in part b at t=27 hrs. d. The DLS data obtained for IgM at different concentrations measured in PBS at 37°C.

Figure 6.
Kinetic analysis of $K_2Q_{23}K_2$ by sedimentation assay. a. Aggregation kinetics of $K_2Q_{23}K_2$ at different concentrations. The reaction labeled "103 μM + S" (blue, right-pointing triangles) contains ~12% by weight of $K_2Q_{23}K_2$ aggregate seeds. b. Time course of spontaneous fibril growth at 215 μM $K_2Q_{23}K_2$ monomer, and of the dissociation of these fibrils, at 37 °C in PBS. The blue dashed line shows the approximate convergence point at about 3 μM, indicating a position of dynamic equilibrium of the forward and reverse reactions. c. Initial aggregation kinetics data of $K_2Q_{23}K_2$ from part a plotted against time^2. d. Log-log plots of initial reaction rates (slopes from part c) versus initial concentration for $K_2Q_{23}K_2$.
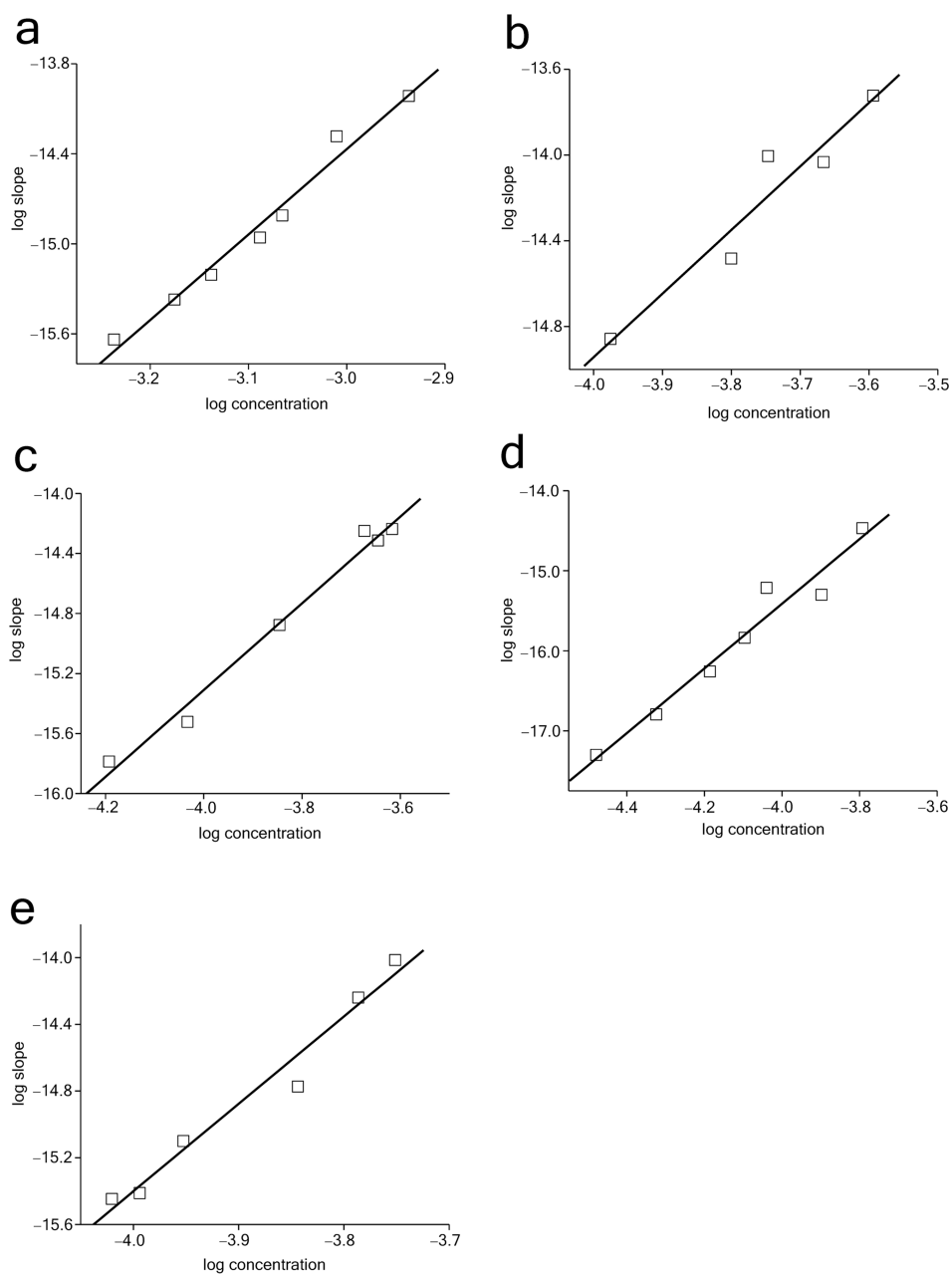
Figure 7.
Log-log plots of initial reaction rates versus initial concentration. Rate data are from time^2 plots (see Supplementary Figure 2). Peptides analyzed are $K_2Q_{18}K_2$ (a), $K_2Q_{27}K_2$ (b), $K_2Q_{26}K_2$ (c), $K_2Q_{25}K_2$ (d) and $K_2Q_{24}K_2$ (e).
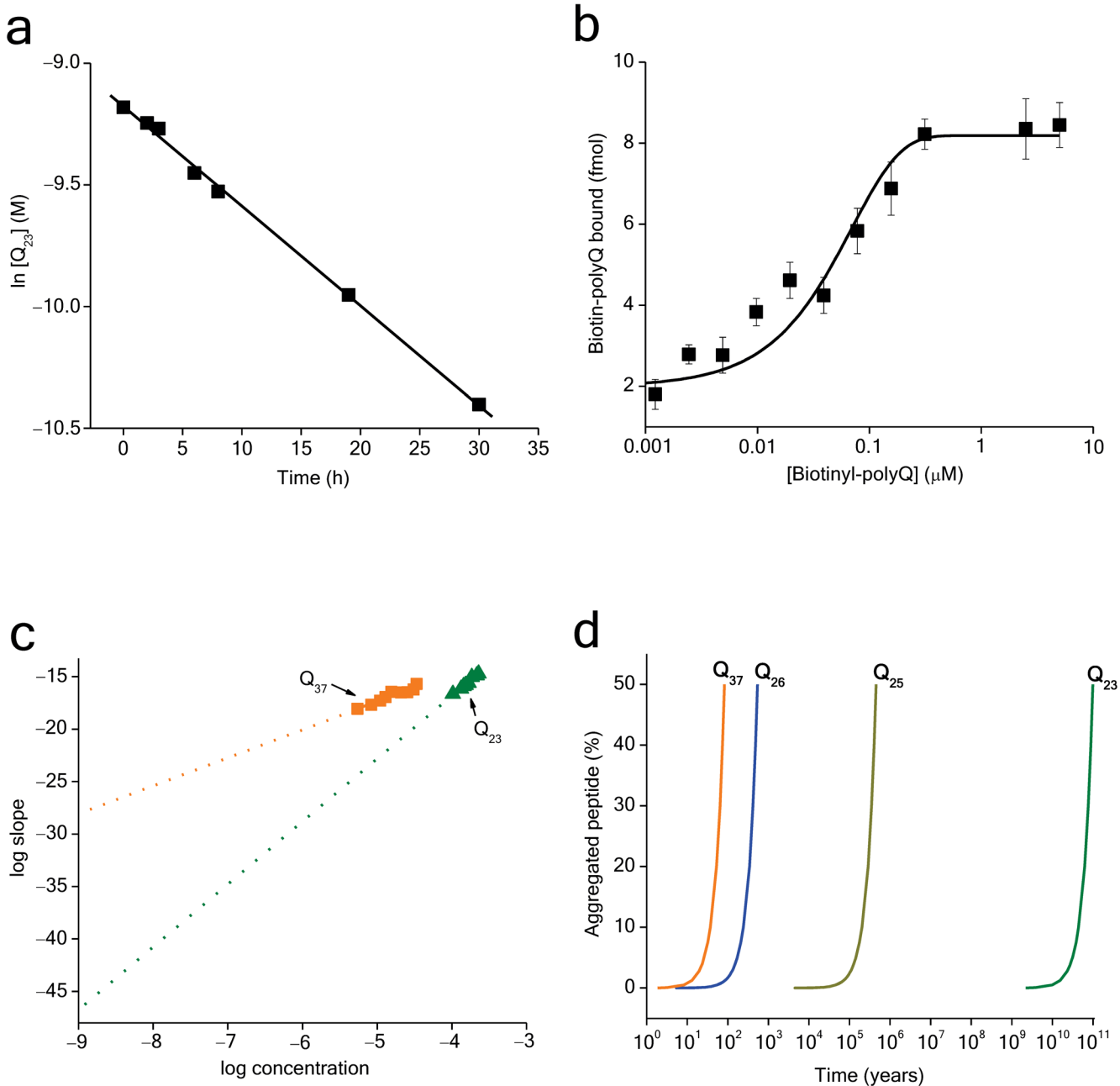
Figure 8.
Further nucleation kinetics analysis of $K_2Q_{23}K_2$. a. Determination of pseudo-first-order elongation rate constant (k^*) from elongation kinetics of $K_2Q_{23}K_2$ seeded with ~12% (w/w) aggregates. b. Determination of the fmoles of biotinylated $K_2Q_{29}K_2$ bound at 25 °C to aliquots of the $K_2Q_{23}K_2$ seed fibril suspension (from panel a) to determine the concentration of growth sites in the seed aggregates (Methods). c. Linear fits of the log-log plot data of $K_2Q_{23}K_2$ and $K_2Q_{37}K_2$ (data from Figs. 6d and 4d, respectively) extrapolated to 1 nM. d. Calculated aggregation kinetics curves for 1 nM of various polyQ peptides using parameters derived from nucleation kinetics analyses.
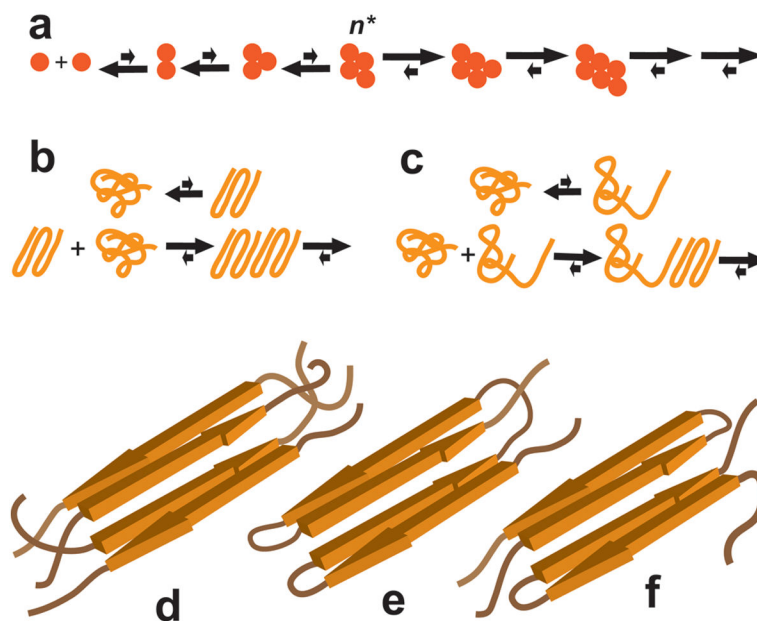
Figure 9.
Models of nucleated growth polymerization. a. Classical thermodynamic model of nucleation, where n* is the critical nucleus. b, c. Two models for monomeric nucleation of polyQ aggregation in which the nucleus is either highly organized (b) or extended (c). d-f. Hypothetical 4-stranded β-sheet model structures for aggregation critical nuclei that are tetrameric (d), monomeric (e), or dimeric (f).

Table 1

Nucleation kinetics analysis on various polyQ peptides[a]

Peptide	Concentrations examined	Slope	R^2	Slope variation[b]	n*
AT7^{NT}Q$_{30}$K$_2$	6	2.7	0.9806	2.61 – 3.23	0.7
SFQ$_{37}$P$_{10}$K$_2$	10	3.0	0.9852	2.92 – 3.08	1.0
K$_2$Q$_{37}$K$_2$	9	2.7	0.9632	2.52 – 2.85	0.7
K$_2$Q$_{27}$K$_2$	5	2.9	0.9264	2.88 – 3.11	0.9
K$_2$Q$_{26}$K$_2$	6	2.9	0.9850	2.77 – 3.17	0.9
K$_2$Q$_{25}$K$_2$	7	4.0	0.9571	3.86 – 4.31	2.0
K$_2$Q$_{24}$K$_2$	6	5.3	0.968	5.03 – 5.54	3.3
K$_2$Q$_{23}$K$_2$	8	5.9	0.9760	5.73 – 6.31	3.9
K$_2$Q$_{18}$K$_2$	7	5.7	0.9793	5.44 – 6.04	3.7

[a]From log-log plots shown in Figures 1, 3, 4, 6 and 7.

[b]In each plot, single data points were removed and the remaining points subjected to linear regression. This operation was repeated for each singly depleted set of data points to yield the range of slope values listed.